The 26th Takayanagi Kenjiro Memorial Symposium

Toward Advanced Imaging Science Creation

Proceedings

November 12, 2024

Hamamatsu Campus,
Shizuoka University, Hamamatsu, Japan
(On-site)

Organized by
Research Institute of Electronics,
Shizuoka University

Cosponsored by
Takayanagi Foundation for Electronics Science and Technology

Preface

Late Prof. Kenjiro Takayanagi began to study an electronic television (TV) system in Hamamatsu Technical College (now Faculty of Engineering, Shizuoka University) in 1924. The Research Institute of Electronics was founded in 1965 based on the Research Laboratory of Electronics (former Takayanagi's Laboratory) attached to Faculty of Engineering, Shizuoka University because Prof. Takayanagi and his coworkers greatly developed the electronic TV system.

The Takayanagi Kenjiro Memorial Symposium is an annual symposium which is organized by the members of the Research Institute of Electronics. It started in 1999 in commemoration of his great development on the system. Various research topics related to imaging science and nanotechnology were reported and discussed by many researchers from not only Japan but also foreign countries.

The 26th Takayanagi Kenjiro Memorial Symposium will be held on-site on November 12, 2024. Plenary Session and Winners of Takayanagi Prize Session are scheduled this year.

I would like to express my sincere appreciation to all of the invited speakers for attending the symposium. I also hope that all participants will enjoy the scientific program and mutual discussion in the Symposium.

Finally I would like to thank the Symposium Chairman, Prof. Masanori Koshimizu and the members of the organizing committee for organizing this wonderful International Symposium.

November, 2024

Masakazu Kimura
Director of Research Institute of Electronics,
Shizuoka University

ORGANIZING COMMITTEE

General Chair

Masakazu Kimura

Symposium Chair

Masanori Koshimizu

Program Chair

Masanori Koshimizu

Local Arrangements

Takayuki Nakano
Daniel Moraru
Tomoaki Masuzawa
Hiroaki Satoh
Hidenori Mimura
Noriyasu Tateishi
Tadanobu Koyama

Treasurer

Masahiro Morimoto

The 26th Takayanagi Kenjiro Memorial Symposium
Research Institute of Electronics, Shizuoka University

Toward Advanced Imaging Science Creation
~ Photonics Technologies across Wide Frequency Range ~

November 12, 2024
S-Port Conference Room, Hamamatsu Campus, Shizuoka University
3-5-1 Johoku, Chuo-ku, Hamamatsu, Japan

9:30 Opening Remarks Masanori Koshimizu (Symposium Chair)
Greetings Kazuyuki Hizume (President of Shizuoka University)
Masakazu Kimura (Director of Research Institute of Electronics, Shizuoka University)

◇Plenary Talks

(Chair: Masanori Koshimizu)

9:40 PL-1. "Research Progress on X-ray Non-Destructive Testing Technology in AIST"
Takeshi Fujiwara (The National Institute of Advanced Industrial Science and Technology (AIST)) …………… 1

10:20 PL-2. "Recent advances in terahertz resonant tunneling diodes"
Safumi Suzuki (Tokyo Institute of Technology, Japan) …………… 3

11:00 Coffee Break

(Chair: Daniel Moraru)

11:10 PL-3. "Growth and device performance of polar and non-polar light emitting diodes on patterned sapphire substrates"
Narihito Okada (Yamaguchi University, Japan) ……………… 5

11:50 PL-4. "2D materials nanophotonics"
Sejeong Kim (University of Melbourne, Australia) …………9

12:30 Lunch Break

◇Lectures by Takayanagi Prize Winners

(Chair: Takayuki Nakano)

14:00 TL-1. “Femtosecond laser lithography: a versatile tool for photonics and materials science”
Vygantas Mizeikis (Shizuoka University, Japan) ……………… 13

14:40 TL-2. “Nanophotonics for Advanced Photonics Devices”
Soh Uenoyama (Hamamatsu Photonics K. K., Japan) ……………… 19

15:10 Coffee Break

(Chair: Hiroaki Satoh)

15:30 TL-3. “Development of Fast Scintillators Based on Hybridization of Polymer and Inorganic Nanoparticles”
Masanori Koshimizu (Shizuoka University, Japan) ……………… 23

16:00 TL-4. “Tuning the functional properties of nanostructures materials for highly efficient optoelectronic devices”
Mani Navaneethan (SRM Institute of Science and Technology, India) ... 27

16:30 Closing Masanori Koshimizu (Symposium Chair)

16:40 Memorial Photo

17:00 Networking @ CO-OP North Cafeteria

Plenary Talks

Research Progress on X-ray Non-Destructive Testing Technology in AIST

Takeshi Fujiwara, Hidetoshi Kato, and Ryoichi Suzuki
National Institute of Advanced Industrial Science and Technology
fujiwara-t@aist.go.jp

Abstract

X-rays are one of the most important methods for non-destructive observation of the interior of objects. This non-destructive inspection technology is widely used in various fields, including industrial applications, academic research, and infrastructure maintenance. At the National Institute of Advanced Industrial Science and Technology (AIST), we are conducting research focused on the development of digital detectors and compact X-ray sources to realize higher resolution, faster processing, wider field of view, and more user-friendly X-ray non-destructive inspection technologies.

In this presentation, we will focus on the achievements of Dr. Takayanagi, who is the namesake of this symposium and a leading figure in display technology, and explore the deep connection between display technologies and X-ray technologies. By reviewing the history of the development of new X-ray imaging detectors at AIST using various technologies, we will provide an in-depth explanation of X-ray inspection technologies related to a variety of display technologies, including cathode-ray tubes, plasma displays, field emission displays, liquid crystal displays, and curved displays.

1. Introduction

Non-destructive testing (NDT) is required across a wide range of applications, from large-scale pipelines and small electronic components to biological samples and geological ores, covering both industrial and academic fields. X-ray-based non-destructive testing is particularly crucial for precisely and non-invasively observing the internal structure of objects in these diverse applications.

In this presentation, I will provide an overview of the research and development we have conducted on X-ray non-destructive testing technologies. Our work has been based on flat panel detectors (FPDs) utilizing oxide semiconductors (IGZO: Indium-Gallium-Zinc-Oxide), which were originally developed for liquid crystal display technology. In addition to the development of the FPD itself, I will delve into our research on key components such as X-ray phosphors, structured scintillators, flexible detectors, and robotic inspection systems that combine these detectors with compact X-ray tubes. These technologies have been developed to address new challenges that traditional methods could not solve.

As shown in Figure 1, these key technologies are closely related to display technologies. In this presentation, I will introduce the technical details of these elements and highlight some of the applied research related to them.

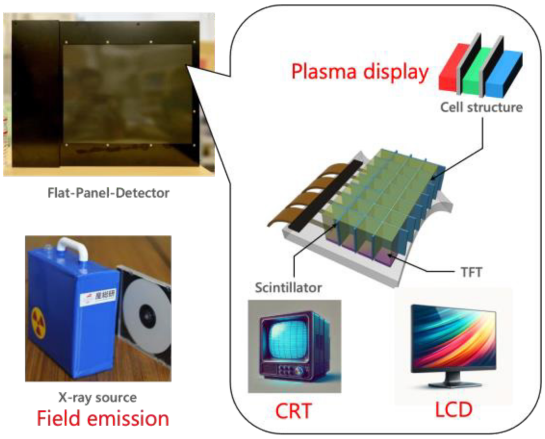

Fig. 1. Relationship between various display technologies and the cutting edge X-ray inspection technologies.

2. X-ray Sources and Detectors

In recent years, the demand for on-site non-destructive testing has grown rapidly. Large pipelines and infrastructure, which cannot be moved, require inspection equipment to be brought to the site for immediate testing. Traditionally, X-ray inspection has relied on systems that utilize X-ray sources weighing over 20 kg and film or imaging plates. However, this method has several challenges, such as the significant labor required, long inspection times, and high radiation doses in the surrounding area.

To address these issues, lighter, more digitalized, and highly sensitive equipment is needed. We focused on field emission technology and developed a compact X-ray source using carbon nanostructures as a field emission electron source.[1] This eliminates the need for a heated filament to release electrons, significantly reducing power consumption. While field emission was originally noted for next-generation display technologies, in X-ray generation, the emitted electrons strike a metal target instead of a phosphor to produce X-rays. By utilizing this technology, we achieved miniaturization and energy efficiency in X-ray sources, which allowed us to integrate these sources into robots for efficient on-site inspections (Figure 2).

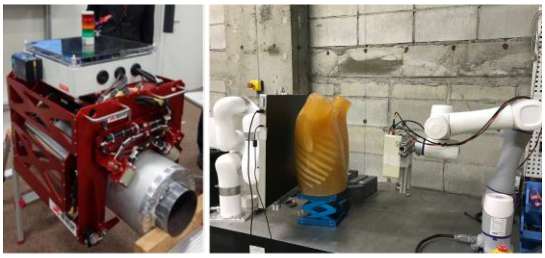

Fig. 2. (Left) A pipeline inspection robot equipped with a compact X-ray source for on-site non-destructive testing. (Right) A robotic X-ray CT system utilizing two robotic arms for precise positioning and scanning of complex objects.

Regarding X-ray detectors, we have developed digital detectors based on Thin-Film Transistor (TFT) technology, which was originally cultivated for liquid crystal displays. Specifically, we designed an indirect flat panel detector (FPD) that uses scintillators, such as GOS or ZnS, materials originally used as phosphors for cathode-ray tubes (CRT). These scintillators are critical in converting X-rays into visible light, and their performance directly impacts the quality of X-ray imaging. Balancing factors such as spatial resolution, detection efficiency, brightness, and afterglow properties is essential for achieving high-quality images.

In this system, X-rays are first converted into visible light by the scintillator, and the light is then transformed into an electric charge by photodiodes. The charges are temporarily stored in capacitors at each pixel and are transmitted through TFTs to the signal lines. This readout process is controlled by gate drivers that activate the TFTs line by line, releasing the stored charge and converting it into digital image signals through an analog front-end circuit. The TFT technology, originally developed for liquid crystal displays, has played a key role in advancing FPDs. By utilizing IGZO (Indium-Gallium-Zinc-Oxide) for TFTs, we improved charge retention, allowing for high signal-to-noise (S/N) ratio images. This has enabled low-dose X-ray inspections, which can be combined with our compact X-ray sources to be applied across various non-destructive testing scenarios[2].

It is a great honor to present these X-ray inspection technologies, which are deeply connected to display technologies, at this symposium named after Dr. Takayanagi, the father of display technology. In this presentation, I will also introduce various applied research achievements that were made possible through the integrated development of X-ray sources and detectors at the National Institute of Advanced Industrial Science and Technology (AIST).

References

[1] Kato, H., Suzuki, R., Wang, J., Ooi, T., & Nakajima, H. (2016). Development of an X-ray tube for irradiation experiments using a field emission electron gun. *Nuclear Instruments and Methods in Physics Research Section A: Accelerators, Spectrometers, Detectors and Associated Equipment*, *807*, 41-46.

[2] Fujiwara, T., Miyoshi, H., Mitsuya, Y., Yamada, N. L., Wakabayashi, Y., Otake, Y., Hino, M., Kino, K., Tanaka, M., Oshima, N., Takahashi, H., (2022). Neutron flat-panel detector using In–Ga–Zn–O thin-film transistor. *Review of Scientific Instruments*, *93*(1).

Recent advances in terahertz resonant tunneling diodes

Safumi Suzuki
Tokyo Institute of Technology
safumi@ee.e.titech.ac.jp

Abstract

In the beyond 5G future wireless communication system, the terahertz (THz) band will be used not only for high data rate communication but also advanced sensing applications. THz oscillators using resonant tunneling diodes (RTDs) are a candidate of THz sources and suitable for these applications due to compactness, high efficiency, and various functionalities. In this paper, recent developments of RTD oscillators and THz applications are reported.

1. Introduction

In Beyond 5G/6G communication system, a use of the terahertz (THz) electromagnetic waves is expected for high-capacity communications but also for sensing applications including imaging and spectroscopic analysis [1-4]. However, the output power of semiconductor THz signal sources is still small, which makes a limit of THz applications.

For the studies of semiconductor THz signal sources, approaches both by optical devices such as quantum cascade lasers (QCLs) and by electronic devices such as diodes and transistors have been conducted [5]. Resonant tunneling diodes (RTDs) are one of the promising candidates for THz sources due to compactness and high-frequency operation [6, 7]. For high-power operation, RTD oscillator arrays have been studied for power combination. In spite of an incoherent operation, an 89-element arrayed oscillator exhibited a high output power of ~0.7 mW at ~1 THz range. Recently, a very high output power of 11.8 mW at 450 GHz was achieved by a 36-element coherent array using mutual injection locking [8]. Besides the power combination using an array, attempts to increase in the output power of a single oscillator have been conducted. In this paper, the recent studies for high-power RTD THz oscillators and applications using developed oscillators will be introduced.

2. High-power RTD terahertz signal sources

RTDs have negative differential conductance characteristics, which can be used for THz oscillation combining with resonator. We employ a thin AlAs barrier and thin InGaAs well RTD structure to achieve high current density and short electron transit time for high frequency and high-power operation. The typical current density is ~10–20 mA/μm^2, and the peak valley current ratio is ~2–4. An n$^+$-InP, which has a high heat conductivity, is employed in conductive bottom layer for efficient heat dissipation.

Our conventional RTD oscillator consists of an RTD having an area of 0.2–1 μm^2 and a slot antenna with a length of ~10–50 μm [6]. The oscillation frequency is roughly determined by the parallel resonance of the RTD capacitance and antenna inductance. Oscillation occurs when the NDC surpasses the radiation and conduction losses. We have achieved a fundamental oscillation of 1.98 THz by a short slot antenna with thick electrode [6].

For high-power THz radiation, various RTD oscillator arrays have been studied. A synchronous operation of the RTD oscillator array is necessary for coherent power combination. Coupling of each array element and control of operating modes in arrayed oscillator are required. For slot-antenna integrated RTD oscillators, we proposed a strong coupling structure via a resistor that allows coherent operation even if there is some frequency variation in each element, performed theoretical analysis, and achieved coherent operation for up to six elements [9, 10]. A two-element device achieved a high output power of 0.77 mW at 530 GHz. Additionally, >1 mW with high radiation directivity was obtained at 400 GHz by double slot-ring structure [11].

We proposed a cavity resonator structure for improving the output power of a single oscillator. This cavity resonator has low loss and low inductance, and can achieve high output power while maintaining the oscillation frequency even with large-area RTDs. However, large-area RTDs generate a lot of heat, which causes a problem of thermal destruction of the device. Therefore, by using InP, which has high thermal conductance, for the lower electrical conduction layer of the RTD instead of low-thermal conductive InGaAs, operations without thermal destruction were obtained due to improvement of heat dissipation [12]. Furthermore, a device combining a cavity resonator and an array technique achieved 0.24 mW at very high frequency of 925 GHz [13].

3. Application

The RTD oscillators have capability of high-speed amplitude modulation, enabling high-speed wireless communication and radar application. Various types of radar systems have been investigated with RTD oscillators, including amplitude-modulated continuous wave (AMCW), subcarrier frequency-modulated continuous wave (FMCW), and subcarrier discrete Fourier transform (DFT) [6, 7]. In these radars, the THz output of RTD oscillators is amplitude-modulated by the subcarrier, and the phase or frequency of the subcarrier is used for ranging. 3D imaging with the AMCW radar and stage scanning was achieved. In subcarrier FMCW radar, two overlapping targets were identified in a single measurement, the real-time measurement of one target was achieved.

Acknowledgements

The authors thank Emeritus Prof. M. Asada of the Tokyo Institute of Technology for stimulating discussions. This work was supported by a scientific grant-in-aid (24H00031) from JSPS, CREST (JPMJCR21C4) from JST, X-NICS (JPJ011438) and ARIM (JPMXP1224IT0018, JPMXP1224IT0019) from MEXT, and the ROHM Company.

References

[1] H. Sarieddeen, N. Saeed, T. Y. Al-Naffouri, and M. Alouini, IEEE Comm. Magazine, 58, 69 (2020).
[2] M. Naftaly, N. Vieweg, A. Deninger, Sensors, 19, 4203 (2019).
[3] G. Valušis, A. Lisauskas, H. Yuan, W. Knap, H.G. Roskos, Sensors, 21, 4091 (2021).
[4] X. Lu, S. Venkatesh and H. Saeidi, China Comm., 18, 175 (2021).
[5] K. Sengupta, T. Nagatsuma, and D. M. Mittleman, Nat. Electronics, 1, 622 (2018).
[6] M. Asada and S. Suzuki, Sensors 21, 1384 (2021).
[7] S. Suzuki and M. Asada, Appl. Phys. Express, 17, 070101 (2024).
[8] Y. Koyama, Y. Kitazawa, K. Yukimasa, T. Uchida, T. Yoshioka, K. Fujimoto, T. Sato, J. Iba, K. Sakurai, T. Ichikawa, IEEE Trans. Terahertz Sci. Technol. 12, 510 (2022).
[9] T. V. Mai, M. Asada, T. Namba, Y. Suzuki, and S. Suzuki, IEEE Trans. Terahertz Sci. Technol. 13, 405 (2023).
[10] S. Suzuki, T. Namba, and T. V. Mai, Int. Symp. Terahertz-Related Devices and Technol., WeP-14, 2023.
[11] S. Endo and S. Suzuki, Appl. Phys. Express, 17, 044001 (2024).
[12] H. Tanaka, H. Fujikata, F. Han, and S. Suzuki, Jpn. J. Appl. Phys. 63, 011004 (2024).
[13] F. Han, T. Shimura, H. Tanaka, and S. Suzuki, Appl. Phys. Express, 16, 064003 (2023).

Growth and device performance of polar non-polar light emitting diodes on patterned sapphire substrate

Narihito Okada
Yamaguchi Univeristy
nokada@yamaguchi-u.ac.jp

Abstract

Gallium nitride (GaN) was grown on a patterned sapphire substrate (PSS) using metalorganic vapor phase epitaxy (MOVPE). The external quantum efficiency of the light-emitting diode (LED) on the PSS reached 49.5% at a current injection of 20 mA. This enhancement in output power was attributed to improvements in both light extraction efficiency and crystalline quality, resulting from the use of PSS. Furthermore, we successfully grew a high-quality semipolar (11–22) GaN layer on an r-plane patterned sapphire substrate (r-PSS). In this study, we report the fabrication of green light-emitting diodes (LEDs) on the (11–22) GaN layer on the r-PSS. The green light emission from the LED on the r-PSS was confirmed, displaying scattered light emission.

1. Introduction

InGaN-based alloy compound semiconductors are highly promising materials for optoelectronic devices, such as high-performance light-emitting diodes (LEDs) and laser diodes. These devices are already widely used in applications like liquid crystal display backlights and traffic lights. The most commonly used substrate for these LEDs is sapphire, however, the flat sapphire substrate exhibits the low light extraction efficiency (LEE) of LEDs caused by the significant difference in refractive index between GaN and sapphire. EQE is the product of internal quantum efficiency (IQE) and LEE. Improvements in LEE have also garnered significant attention, with various methods demonstrated to enhance LED performance. Many types of patterned sapphire substrates have been developed and successfully applied to fabricate high-efficiency LEDs, as they enhance both IQE and LEE.

In addition, semipolar and nonpolar LEDs have been studied for their ability to reduce the quantum confined Stark effect (QCSE), which is believed to help address the "green gap" problem. In recent years, visible light communication (VLC) has attracted considerable attention as an advanced high-speed communication technology, expected to meet the increasing capacity demands of 6G networks. Semipolar and nonpolar LEDs demonstrate faster radiative recombination lifetimes, making them suitable for VLC applications requiring high-speed communication.

To achieve semipolar or nonpolar GaN, we have focused on growing GaN from the sapphire sidewall of a PSS, which allows for larger diameters due to the use of sapphire. The crystalline quality of GaN films grown this way is higher than those formed using conventional epitaxial lateral overgrowth techniques. We found that GaN can be selectively grown from only the sapphire sidewall of r-PSS. This selective growth does not require a growth-inhibiting mask, such as SiO_2. In previous studies, selective-area growth from the sapphire sidewall of r-PSS was observed due to forming a GaN nucleation layer predominantly on the sapphire sidewall.

In this paper, we describe the growth of c-plane GaN on a random-cone (RC) PSS and semipolar {11-22} GaN on the r-PSS. Furthermore, we fabricated LEDs based on these structures and characterized the performance.

2. Results and discussion

A. *c*-plane GaN on RC-PSS [1]

To simplify the fabrication process, one potential method is natural lithography. We grew GaN on a random-cone (RC) PSS and investigated the growth mechanism. An RC-PSS was fabricated by natural lithography an inductively coupled plasma reactive ion etching (ICP-RIE). Microspheres made of polystyrene with a diameter of 4 μm were deposited on the sapphire substrate as a mask. Then, the sapphire substrate was etched by ICP-RIE. BCl_3 was used as the etching gas. When the microspheres were etched by ICP-RIE, they deformed into a cone shape owing to the etching and annealing effects. Subsequently, cone-shaped masks were etched away with the etching of the sapphire substrate.

Consequently, an RC-PSS was obtained. Figure 1(a) shows a bird's-eye view scanning electron microscopy (SEM) image of the RC-PSS. The height and diameter were 1.5 and 4 mm, respectively. It was observed that the cones were arranged randomly. A GaN layer was grown on the RC-PSS by metalorganic vapor phase epitaxy (MOVPE). Conventional growth conditions of a GaN layer on a sapphire substrate were adopted: a low-temperature GaN buffer layer and a growth temperature of 1150 °C.

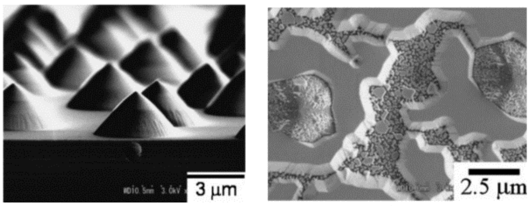

(a) (b)

Fig. 1. SEM images of bird's-eye view of (a) RC-PSS and (b) initial growth of GaN grown for 12 min. Cones were randomly arranged on sapphire substrate by natural lithography.

GaN grew from only a flat area and predominantly grew around the cones despite the LT-buffer layer deposition on the surfaces of the cones. To clearly observe the growth mode, a magnified SEM image of GaN grown for 12 min is shown in Fig. 1(b). The growth mode of the GaN layer was affected by the cones. The inclination angle of the sidewall of the random-cone structure was approximately 43^{o} and no specific plane of sapphire appeared because of the cone shape. Thus, it was assumed that nonreactive vapor sources of Ga and N on the cones diffused around the cones, which led to a higher growth rate of GaN around the cones compared with that in the flat area away from the cones. Finally, the large GaN grains formed around the cones covered the small GaN grains formed in the flat area, and the GaN layer coalesced perfectly. These results indicate that epitaxial lateral overgrowth and selective lateral growth occurred on the RC-PSS. In the case of the growth of the GaN layer on the RC-PSS, the growth conditions of the high-temperature GaN layer were not changed and a flat GaN layer was obtained.

Then, we fabricated LED devices on the RC-PSS (RC- LED) as shown in Fig.2 (a) and a flat sapphire substrate (std-LED). Figure 2 (b) shows the light output power and EQE in relation to the injection current of the RC-LED. The output power of the LED was measured using an integrated system at forward currents from 0.5 to 100 mA. The wavelength of the RC-LED was approximately 420 nm. The output power of the RC-LED was approximately 1.34 times larger than that of the std-LED with the same LED structure at a current injection of 20 mA. The light output power and EQE of the RC-LED were 29.6 mW and 49.5%, respectively, at a current injection of 20 mA. The EQE decreased markedly with increasing injection current, especially in the lower- injection-current region. The maximum EQE is 75.1% at 0.5 mA, which is 50% higher than the EQE at 20 mA. In the case of the blue LED, the high-efficiency LED requires a constant EQE in the lower-injection-current region. Hence, there is room for optimizing the LED structure. The IQE of the RC-LED was evaluated from the relationship between excitation power density and temperature-depend- ent photoluminescence under selective excitation conditions using a dye laser with a 385 nm. IQE was estimated to be approximately 57%, which was the maximum PL quantum efficiency at room temperature, assuming that the peak PL quantum efficiency at a cryogenic temperature of 7 K is 100%. LEE was estimated to be 86.8% because EQE is a product of IQE and LEE. This LEE obtained using the RC- PSS was high. Thus, it is concluded that the RC-PSS is useful for achieving a high LEE of InGaN/GaN LED.

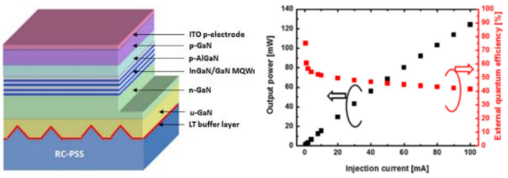

(a) (b)

Fig. 2. (a) Schematic structure of LED on RC-PSS and (b) RC-PSS and (b) Output powers and external quantum efficiencies of RC-LED as a function of forward-bias current.

B. {11-22} GaN on r-PSS [2, 3]

A groove-patterned 0.5° -off r-PSS was prepared. The groove was as deep as 1 μm. The groove and terrace widths were both 3 μm. The period of the pattern was 6 μm. Figure 3(a) shows a schematic of the principle growth mechanism of {11-22} GaN on the r-PSS. The angle of 57.6° between r-plane sapphire and c-plane sapphire is similar to that of 58.4° between the {11-22} plane of GaN and the c-plane of GaN, indicating that the r-plane sapphire is the appropriate substrate for the growth of the {11-22} GaN layer. Furthermore, a 0.5°-off-angle r-plane sapphire substrate was used, and the mismatch angle of each c-axis was as small as 0.3°. The GaN layer was grown on the r-PSS by MOVPE. It is reported that it is easy to form the {11-22} facet under high-pressure and low-V/III-ratio conditions by selective area growth and epitaxial lateral overgrowth of c-plane GaN on a GaN template with a [1-100] SiO_2 stripe mask. The semipolar {11-22} GaN layer was directly grown on the r-PSS without the SiO_2 mask. Fig. 3(b) shows the cross-sectional SEM images of the semipolar {11-22} GaN layers grown for 3 h at 1000 °C. The semipolar {11-22} GaN layer grown on r-PSS has a smooth surface and step bunching was not observed. In the case of the growth of the semipolar {11-22} GaN layer on the r-PSS, step bunching related to c-plane sapphire does not influence the morphology of the {11-22} surface. This is beneficial for the growth of nonpolar or semipolar GaN layers from the sidewall of sapphire substrates, since it is difficult to expose the exact c-plane sapphire sidewall by ICP-RIE.

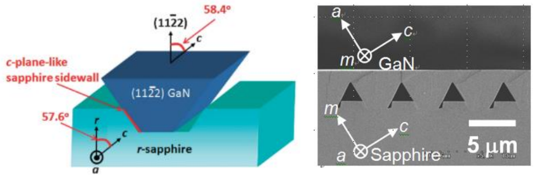

(a) (b)

Fig. 3. (a) Schematic of growth of semipolar (1122) GaN layer on maskless patterned r-plane sapphire substrate. (b) Cross-sectional SEM images of semipolar {11-22} GaN grown at 1000 °C.

A {11-22} LED was fabricated on the r-PSS. The (11–22) LED was composed of an n-type GaN:Si layer, four-period InGaN/GaN MQWs, a p-type AlGaN:Mg electron blocking layer, and a p-type GaN:Mg layer. A c-LED of the same structure was fabricated on a c-plane flat sapphire substrate for comparison. Electroluminescence (EL) was measured under a continuous-wave operation. Figure 4 shows the on-wafer light-emission images of the green-LEDs on the r-PSS and flat c-sapphire substrate measured using a probing system. The scattered green light emission was confirmed from the {11-22} LED fabricated on the r-PSS, in contrast to the spot light emission of the c-LED. This scattered light emission of the {11-22} LED on the r-PSS was achieved through the effects of the patterned sapphire and air void structures. The green light emission with a peak emission wavelength of 506.4 nm was confirmed at an injection current of 20 mA. Figure 5 shows peak emission wavelength as a function of injection current. The {11-22} LED on the r-PSS had a small blue shift compared with the conventional c-LED. The blue shift of this LED from 20 to 100 mA was 8.9 nm, while that of the c-LED was 17.3 nm. This result indicates that the difference in peak shift between {11-22} LED and c-LED is attributed to a reduction in QCSE.

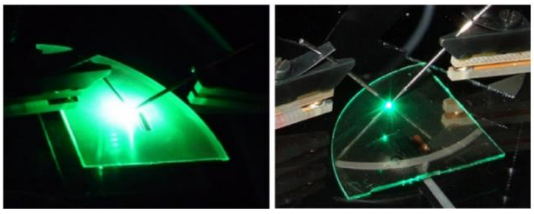

(a) (b)

Fig. 4. On-wafer light-emission images of green LED on (a) {11-22}GaN on r-PSS and (b) c-plane GaN on flat c-sapphire substrate measured using probing system. The LED on the r-PSS exhibits scattered light emission.

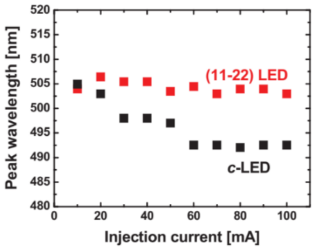

Fig.5 Peak emission wave- length as a function of injection current for {11-22} LED on the r-PSS and c-LED.

3. Summary

We grew a GaN layer on an RC-PSS by natural lithography without photolithography and investigated the GaN growth mechanism. ELO on cones and SAG around the cones were observed by SEM. The RC-PSS was observed to be effective for reducing the number of threading dislocations in the GaN layer. The EQE of the LED on the RC-PSS was 49.5% at a current injection of 20 mA. The LEE of the RC- LED was estimated to be 86.8%.

We demonstrated a semipolar {11-22} GaN layer on the r-PSS with a flat surface and high-crystalline quality. The scattered green light emission was confirmed from the LED fabricated on the r-PSS. It was confirmed that air void structures are one of the advantages of the r-PSS .

References

[1] N. Okada, T. Murata, K. Tadatomo, H. C. Chang, and K. Watanabe, Jpn. J. Appl. Phys. 48, 122103 (2009).

[2] N. Okada, A. Kurisu, K. Murakami, and K. Tadatomo, Appl. Phys. Express 2, 091001 (2009).

[3] N. Okada, K. Uchida, S. Miyoshi, and K. Tadatomo, Phys. Stat. Solidi (a) 209, 469 (2012).

All-2D material photonic devices

Sejeong Kim
University of Melbourne
sejeong.kim@unimelb.edu.au

Abstract

Two-dimensional (2D) materials are extensively used in almost all scientific research areas, from fundamental research to applications. Initially, 2D materials were integrated with conventional non-2D materials having well-established manufacturing methods. Recently, the concept of constructing photonic devices exclusively from 2D materials has emerged. Various devices developed to date have been demonstrated based on monolithic or hetero 2D materials. In this review, photonic devices that solely consist of 2D materials are introduced, including photonic waveguides, lenses, and optical cavities. Exploring photonic devices that are made entirely of 2D materials could open interesting prospects as they enable the thinnest devices possible because of their extraordinarily high refractive index. In addition, unique characteristics of 2D materials, such as high optical anisotropy and spin orbit coupling, might provide intriguing applications.

1. Introduction

Two-dimensional (2D) materials have become important in almost all fields of research, including electronics, photonics, and material engineering. To this point, numerous favorable characteristics of 2D materials have been reported. For instance, graphene has exceptionally high thermal and electrical conductivities, and its electrical conductivity is comparable to or slightly higher than that of silver. Transition metal dichalcogenides (TMDs) have a direct energy bandgap in their monolayer form, which enables the use of 2D materials as a light emitting material. Such thin light emitting materials are traditionally manufactured by growing a thin semiconductor layer, i.e., a quantum well, with a smaller energy bandgap. 2D light emitting materials can be combined with any other materials, whereas quantum well growth is constrained by lattice match between the substrate and the quantum well. Moreover, 2D materials are now promising candidates for quantum light sources and optoelectronic devices.

In the early stages of 2D material-based devices, particularly for photonics applications, 2D materials were integrated with devices made of conventional bulk materials with well-established fabrication technology, such as Si, SiN, SiO_2, etc. It was only recently that scientists have begun to develop optical devices using exclusively 2D materials. This raised interesting research questions such as can a monolayer guide light? Can layered materials serve as optical cavities? Exploring all-2D material photonic devices will generate fruitful discussions.

Here, we provide an overview of recent developments in the use of stand-alone 2D materials for optical components. Multiple photonic devices are presented using solely 2D materials and various functioning optical devices are demonstrated. This includes the vast majority of essential optical components, such as waveguides, cavities, and modulators. All-2D material devices were combined with emerging research areas: metaphotonics and Mie-tronics, which are covered in this review. Studying monolithic 2D photonic devices necessitates precise optical parameters, such as refractive index and absorption, which were recently determined by experimental measurements of exfoliated 2D materials. Perspectives and opportunities on stand-alone 2D materials devices are discussed.

2. Light guiding in 2D materials

A waveguide is an essential component of all integrated photonic circuits. In order to guide light, photonic waveguides typically have a thickness of λ/2neff. As the dimension of the waveguide decreases, light is weakly guided and susceptible to bending loss. To create thin waveguides, a high refractive index is required; however, the refractive index of common semiconductors is restricted between 2 to 4 at visible wavelength, and often declines as wavelength increases. To obtain a high refractive index, a material having excitonic resonance at visible wavelengths can be used. In this regard, TMDs are promising materials not only because they have excitonic resonance at visible wavelength but also their excitonic resonance is strong. This is because of the reduced dielectric screening and enhanced Coulomb interaction. Fig. 1a shows the binding energy and optical bandgap of different 2D materials in their bulk and monolayer forms. The high binding energy indicates higher stability and a high refractive index, which allow for ultrathin photonic devices.

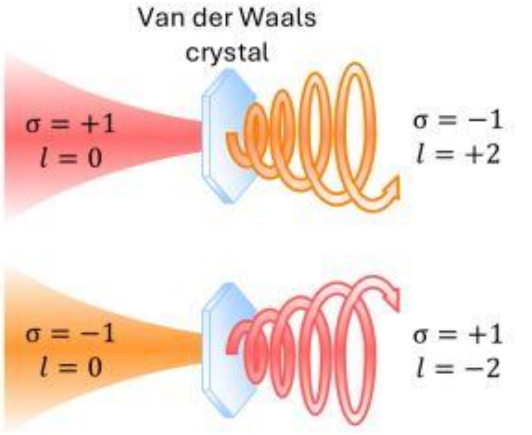

Fig. 1. (Top) left-handed circularly polarized (LCP) light (σ = +1), initially without orbital angular momentum (OAM) (l = 0), is incident onto a vdW crystal along its extraordinary axis, i.e. z-axis. As the beam propagates through the material, it is converted into a right-handed circularly polarized (RCP) beam (σ = −1) with an OAM mode of +2. (Bottom) When an RCP beam is incident, vdW crystal converts it into an LCP beam with an OAM mode of −2 (l = −2).

3. Optical vortex generator

An optical vortex beam has attracted significant attention across diverse applications, including optical manipulation, phase-contrast microscopy, optical communication, and quantum photonics. To utilize vortex generators for integrated photonics, researchers have developed ultra-compact vortex generators using fork gratings, metasurfaces, and integrated microcombs. However, those devices depend on costly, time-consuming nanofabrication and are constrained by the low signal to-noise ratio due to the fabrication error. As an alternative maneuver, spin-orbit coupling has emerged as a method to obtain the vortex beam by converting spin angular momentum (SAM) without nanostructures. Here, we demonstrate the creation of an optical vortex beam using van der Waals (vdW) materials. The significantly high birefringence of vdW materials allows generations of optical vortex beams with high efficiency in a sub-wavelength thickness. In this work, we utilize an 8-µm-thick hexagonal boron nitride (hBN) crystal for the creation of optical vortices carrying topological charges of ±2.

References

[1] S. Kim, *Nanoscale Adv.*, 2023, **5**, 323-328
[2] J. Jo, S. Byun, M. Bae, J. Wang, H. Chung, S. Kim, *arXiv*:2408.12061

Lectures by Takayanagi Prize Winners

Femtosecond laser lithography: a versatile tool for photonics and materials science

Vygantas Mizeikis
Research Institute of Electronics, Shizuoka University
mizeikis.vygantas@shizuoka.ac.jp

Abstract

We describe application of the femtosecond laser lithography technique in the fields of photonics and materials science. In photonics, using two-photon polymerization process in photoresists, 3D photonic crystals and optical metasurfaces that allow to control emission, absorption and propagation of light by exploiting sub-wavelength scale interaction between light waves and the finely patterned structure were realized. In materials science, femtosecond laser pulses were used to induce permanent modification in sapphire Al_2O_3 crystals by extremely high temperature and pressure conditions, leading to first known experimental synthesis of a new ultra-dense phase aluminum nanocrystals.

1. Introduction

Femtosecond laser lithography uses tightly focused powerful femtosecond laser pulses to modify materials and create micro and nanostructures that are useful for applications and fundamental studies. In photonics, two-photon polymerization [1] in photoresist induced by the femtosecond laser pulses allows realization of 3D periodic micro and nanostructures enabling the control over emission, absorption and propagation of light by exploiting sub-wavelength scale interaction between the light wave and the finely patterned structure [2]. In photonics, using femtosecond laser lithography technique we have realized 3D photonic crystals [3] exhibiting a range of optical functionalities not found in ordinary materials: structural color phenomenon, spatial localization along propagation direction, and optical birefringence [4] were realized. In addition, by combining femtosecond laser lithography and metallization techniques, metalo-dielectric optical metasurfaces exhibiting perfect absorption of radiation at infrared wavelengths were demonstrated [5]. In materials science, femtosecond laser lithography was used to induce permanent modification in sapphire Al_2O_3 crystals due to extremely high temperature and pressure in hot electron-ion plasma ignited by the laser pulses [6]. This has led to the first experimental synthesis of a new ultra-dense phase aluminum [7]. By allowing to conduct these studies in an ordinary laboratory without the requirement for cleanroom environment, vacuum conditions, aggressive chemicals, and other expensive or dangerous equipment/substances, femtosecond laser lithography emerges as a valuable tool for applied and fundamental science.

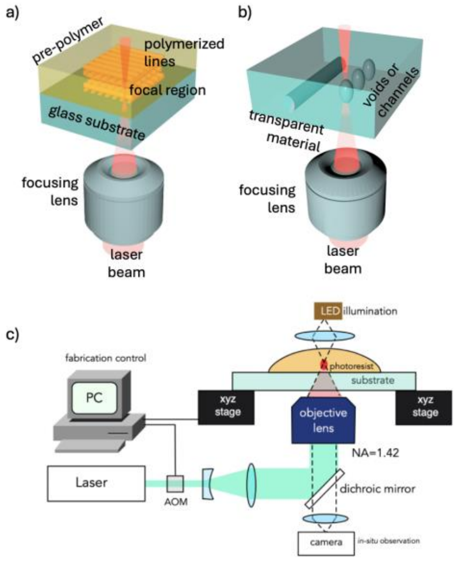

Fig. 1. Femtosecond laser lithography using (a) two-photon polymerization in photoresist, (b) laser-induced local damage in transparent solids, (c) schematic image of the opto-mechanical setup used.

2. Implementation of femtosecond laser lithography

Figure 1 summarizes the principles and shows practical implementation of femtosecond laser lithography experiments used in our studies. The use of two-photon polymerization (TPP) is illustrated in Fig. 1(a). Pulses of a femtosecond laser are tightly focused in the bulk of pre-polymer material (usually organic photoresist), and induce two-photon absorption (TPA) selectively in the focal region of the beam, leading to TPA. By carefully controlling the laser exposure dose, due to the non-linear nature of absorption, the size of the photopolymerized region can be reduced well below the diffraction-limited size of the focal region. Typical lateral size of the photopolymerized region achievable using oil-immersion microscope lens is ≈200 nm and can be reduced further below 100 nm[8]. Thus, focus of the femtosecond laser beam can be regarded as a tip of very sharp pen with which one can draw fine photopolymerization patterns in photoresist by 3D translation of the focal region (or the sample) in space. Subsequently, the unexposed pre-polymer can be dissolved using chemical development, leaving only the polymerized micro or nanostructure having the desired geometry. Thus, this approach is similar to 3D printing but with spatial resolution increase by about 10,000 times. We have used this approach for the fabrication of 3D photonic crystals and optical metasurfaces.

Femtosecond laser lithography using laser-induced localized damage is illustrated in Fig. 1(b). In this case the original medium, which can be a crystalline or disordered optically transparent solid, becomes permanently modified by optical damage or near-damage conditions achieved in the focal region due to the high instantaneous laser power. At sufficient laser exposure dose optical damage occurs as explosive dielectric breakdown, leaving tiny voids in the initial material [9]. Photomodified region around the void may contain strongly modified material, such as new phases of the initial material created by short-lived extreme temperature and pressure conditions (ETP) during the laser pulse. This method is widely used in science and technology for realization of 3D optical memories and aveguides, etc., but here we find a new application for the creation of new phases of materials.

Figure 1(c) shows practical implementation of the opto-mechanical setup used for femtosecond laser lithography experiments. The laser source was Carbide fs laser system (Light Conversion) emitting pulses having a temporal width of 300 fs and maximum pulse energy of 80μJ at the central wavelength of 515 nm and an adjustable repetition rate of up to 1MHz. 3D nanopositioning system (Aerotech) was used for the sample translation during fabrication. Geometry of the exposed structure and its exposure dose were controlled using 3DPoli software package. This setup enabled the performance of femtosecond laser lithography using either TPP or laser-induced damage mechanisms, depending on the need. For fabrication of 3D photonic structures exploiting TPP process photoresists SZ2080™ [10] and SU-8 deposited on glass substrates were used. For fundamental studies using laser-induced damage, sapphire (Al_2O_3) crystals in the form thin polished slabs (d≈80μm) were used.

3. Photonic structures fabricated using femtosecond laser lithography

Photonic crystals [11] are structures composed of transparent dielectric material having periodic modulation of their refractive index in space, with period comparable to the optical wavelength (Fig. 1(a)). Due to their periodicity, spectral bands characterized by a strong optical reflectivity ($R≈1$) and vanishing transmittivity ($T≈0$) evolve in photonic crystals. The corresponding spectral range is also called a photonic band gap (PBG) in direct analogy with forbidden bandgap existing for electrons in periodic crystalline solids. Photonic crystals exhibiting PBG at well-define wavelength in the visible spectral range will exhibit distinct color corresponding to the PBG central wavelength upon observation. Using femtosecond laser lithography technique we have fabricated arrays of 3D photonic crystals having so-called woodpile architecture [3], and systematically varied their structural parameters (lattice period and thickness of dielectric nanorods composing the photonic crystal). Figure 2(b) shows optical microscopy image of one such array clearly indicating the structural color variation within array. The entire array was fabricated within a few hours in an ordinary laboratory room. Structural color

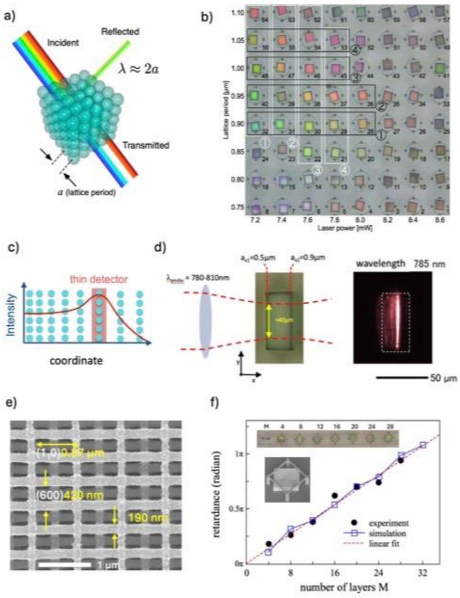

Fig. 2. (a) schematic depiction of a 3D photonic crystal and its optical properties, (b) 3D photonic crystals exhibiting structural color, (c) schematic principle of photon localization in a chirped photonic crystal, (d) experimental demonstration of localization using 3D photonic crystal, (e) close-up image of an anisotropic and optically birefringent 3D photonic crystal, (f) dependence of its phase retardation on the crystal thickness.

is not related to absorption or emission of light by dyes and pigments and occurs purely due to reflection and interference of light in the periodic structure. Consequently, it is highly sought in many applications that require non-chemical, non-fading colors.

Figure 2(c) schematically depicts another attractive application of photonic crystals that have spatial variation of their lattice period (also called chirp) along one direction. In such structure PBG wavelength varies in space, and light waves can propagate in the photonic crystal up to certain penetration depth before encountering strong reflectivity due to the PBG. At this point wave propagation becomes slowed down and reversed, leading to the local enhancement of intensity (Fig. 2(c)) [12]. This circumstance can be used to enhance sensitivity of photodetectors by embedding them at the corresponding location in the structure (this task will be addressed in future). Using femtosecond laser lithography we have fabricated a 3D woodpile photonic crystal with chirped lattice period and visualized its capability to localize the optical field. Left part of Fig. 2(d) shows top-view optical microscopy image of the fabricated sample. The lattice chirp was imposed along the x-axis direction during fabrication, and the probing laser beam was propagated through the sample along the same direction. Right part of Fig. 2(d) shows experimental visualization of the optical field localization in the structure at the wavelength of 785nm.

3D photonic crystals in photoresist also enable to create artificial birefringence, called form birefringence. In order to achieve it the photonic crystal lattice must be made asymmetric, leading to the structural anisotropy, optical anisotropy, and birefringence. Figure 2(e) shows close-up image of a woodpile photonic crystal which has spatial anisotropy due to its different lattice periods along x and y-axis directions. Figure 2(f) shows the measured birefringent phase retardation at the wavelength of HeNe laser (632 nm) as a function of the structure thickness (number of layers in woodpile photonic crystal). As can be seen, it is possible to achieve quarter-wave and half-wave phase retardation levels using asymmetric photonic crystal structures [4]. These retardation levels are needed in many applications. Using femtosecond laser lithography one can thus realize super-compact half- and quarter-wave plate elements and integrate them into photonic integrated circuits.

4. Femtosecond laser lithography as a tool for Materials Science

At extreme pressures and temperatures, such as those inside planets and stars, common materials form new dense phases with compacted atomic arrangements and unusual physical properties [13]. The synthesis and study of new phases of matter at pressures above 100 GPa and temperatures above 10^4 K —warm dense matter—may reveal the functional details of planet and star interiors and may lead to materials with extraordinary properties. Static pressure of up to MPa and GPa (10^6-10^9 Pa) is achievable in a diamond anvil cell (DAC) by compressing the sample between two super-hard diamond crystals, simultaneously heating the sample by a laser beam. Even higher (up to 100 TPa) pressure is achievable using dynamic shock-wave compression in which primary source (gas gun, conventional or nuclear explosion, or ablation impact of a kilo/mega-class energy laser) generates a powerful shock-wave transferred to the sample. Thus, the creation of extreme pressure and temperature (EPT) conditions requires the experimental equipment that is bulky, expensive, and often dangerous to operate.

Application of femtosecond laser lithography for the realization of EPT conditions is illustrated schematically in Fig. 3(a,b). A femtosecond laser pulse is focused inside the transparent initial material inducing its dielectric breakdown causing its optical breakdown at the focus. Tight focusing of a laser pulse using a lens with numerical aperture (NA) of >1.3 can deposit a high energy density of several MJ/cm^3 into a sub-micron sized region for typical pulse duration of ~100 fs and a low single pulse energy of ~100 nJ [14]. This is several times higher than the strength of any material, and causes the solid to superheat and form a plasma. The plasma is initially (within ~ 100 fs) localized at the focus but subsequently explodes and generates a powerful shock wave that expands out of the focal volume and compresses the hot material against the surrounding cold pristine surroundings, removing material from the center and forming a void surrounded by a densified shell (Fig. 3(a)). The void-shell system is permanently preserved by fast quenching which occurs within ~ 1 ns after the excitation. Magnitude of the shock wave depends on the properties of material, for example Young modulus, and is estimated to reach pressures over 100 Megabar (1 TPa) in hard materials, such as SiO_2 and Al_2O_3. Diameter of void and thickness of densified shell are on the order of few hundreds of nanometers. The compressed shell can potentially contain the new modified crystalline phases of material. This is a particular advantage over other existing methods, since material compressed by the shock wave remains confined in compressed state in a strongly localized region inside a bulk of pristine crystal and is permanently available for investigations. Although the total affected volume per void-shell remains very small, it is sufficient for characterization using currently available X-ray diffraction (XRD) techniques.

To prepare the samples, we have performed laser patterning of sapphire slabs with periodic 3D arrays of laser-generated voids and densified shells. This ensured larger volume of material probed by a collimated X-ray beam during characterization. The characterization was carried out using angle-dispersive X-ray diffraction at HPCAT beamline 16-BM-D of the Advanced Photon Source, Argonne National Laboratory. The main experimental findings are summarized in Fig. 3(b,c). As can be seen from Fig. 3(b),

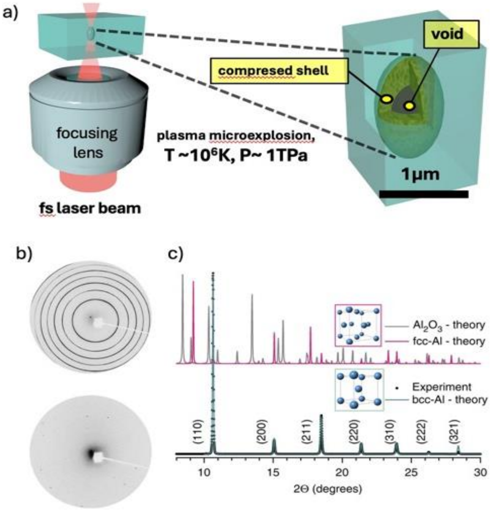

Fig. 3. (a) schematic depiction laser-induced microexplosion in a solid, (b) raw XRD spectra taken in laser processed sample area (top) and pristine area (bottom), (c) azimuthally-integrated XRD spectra and their comparison with theory.

pronounced XRD rings can be seen from the laser-patterned regions of sapphire (top), but no signal could be detected from pristine regions (bottom). Radially integrated XRD pattern from the laser-patterned area is shown in Fig. 3(c). From the seven diffraction peaks corresponding to the rings one can determine the lattice period and symmetry. The experimental spectrum was compared with known patterns of existing and theoretically predicted phases of Al_2O_3 but no satisfactory match could be obtained. This is illustrated in Fig. 3(c) where theoretical XRD pattern of ambient sapphire show strong differences from the experimental observations. Further examination focused on the possibility of constituent atoms (Al or O) forming new ambient or compressed phases has revealed a perfect match to the theoretically expected pattern for pure aluminum with a bcc crystal lattice (bcc-Al phase, space group Im3m) with a lattice constant a=2.864 angstrom [7]. The present study gives an experimental evidence of the new bcc-Al phase which was predicted to exist at high pressure, but has not been confirmed previously. Most likely this phase is formed under EPT conditions when sapphire becomes decomposed into Al and O atoms due to their different mobilities, and spatial separation between these atoms develops before the onset of cooling. Confined microexplosions induced during the femtosecond laser lithography process offer a strategy to create and a simple method for tabletop studies of materials under extreme pressure and temperature conditions.

5. Conclusions

Our studies have demonstrated high versatility of femtosecond laser lithography technique. In photonics it enables 3D rapid prototyping of nano- and micro-structures in a manner akin to the macro-scale 3D printing, but with much higher spatial resolution. In Materials Science it enables realization of extreme pressure and temperature conditions, and synthesis of new phases of materials using accessible and safe desktop experiments.

Acknowledgements

This work was carried out in close collaboration with domestic and international research groups. In particular, contributions by dr. S. Juodkazis (Swinburne University of Technology), dr. A. Vailionis (Stanford University), dr J. Morikawa (Tokyo University of Technology), dr. A. Saito (Osaka University), and dr. A. Ono (Shizuoka University) are acknowledged.

References

[1] S. Kawata, et al. *Nature* **412** (2001) 697-698.
[2] M. Malinauskas et al. *Light: Science & Applications* **5** (2016) e16133-14.
[3] V. Mizeikis et al. *Opt. Lett.* **29** (2004) 2061-2063.
[4] D. Gailevičius et al. *Opt. Lett.* **48** (2023) 5775-5778.
[5] I. Faniayeu & V. Mizeikis *Opt. Mater. Express* **7** (2017) 1453-1410.
[6] S. Juodkazis et al. *Phys. Rev. Lett.* **96** (2006) 166101.
[7] A. Vailionis et al. *Nature Comm.* **2** (2011).
[8] S. Juodkazis et al. *Nanotechnology* **16** (2005) 846-849.
[9] S. Juodkazis et al. *Appl. Phys. Lett.* **88** (2006) 201909.
[10] A. Ovsianikov et al. *ACS nano* **2** (2008) 2257-2262.
[11] E. Yablonovitch. *Scientific American* **47** (2001) 48-55.
[12] Z. Hayran, Kurt, H. & K. Staliunas. *Scientific Reports* **7** (2017) 1-10.
[13] D. M. Teter, R.J. Hemley, G. Kresse & J. Hafner. *Phys. Rev. Lett.* **80** (1998) 2145-2148.
[14] Gamaly et al. *High Energy Density Physics* **8** (2012) 5.

Nanophotonics for Advanced Photonic Devices

Soh Uenoyama
Hamamatsu Photonics K.K.
so.uenoyama@crl.hpk.co.jp

Abstract

Silicon photomultipliers (SiPMs) are essential for applications such as Time-of-Flight Positron Emission Tomography (TOF-PET), high-energy physics (HEP), and Light Detection and Ranging (LiDAR), due to their ultra-sensitive photon detection capabilities. These applications require improved SiPM performance. SiPMs consist of many two-dimensional SPAD (single-photon avalanche diode) arrays. Each SPAD includes trench areas that not only function as cross-talk blockers but also reduce the photosensitive area. Illuminating these trench areas degrades the performance of the SiPM. To address this issue, I introduced a metalens approach that redirects incident photons away from the trench areas and towards the photosensitive regions of the SPAD. I successfully fabricated a metalens array aligned with the SPAD pixels without errors, demonstrating a 70% improvement in photodetection efficiency (PDE) at the near-ultraviolet wavelength range compared to the SiPM without the metalens. Additionally, I will introduce other nanophotonics techniques tailored to different wavelengths and applications to further enhance photodetection sensitivity.

1. Introduction

Recently, nanophotonic technologies have advanced significantly due to improvements in fabrication techniques and the evolution of computer technologies. These advancements are increasingly being applied to photodetectors to enhance its photosensitivity while maintaining a compact device size. However, since the requirements for improving photodetector sensitivity vary depending on the wavelength and application, it is essential to design nanophotonic materials and mechanisms specifically tailored to each wavelength and application.

In scintillation applications such as time-of-flight positron emission tomography (TOF-PET) [1] and high-energy physics (HEP) experiments [2], silicon photomultipliers (SiPMs), which contain a lot of two-dimensional arrays of SPADs (Single-Photon Avalanche Diodes), has commonly been used. However, SPADs typically include trench areas that, while reducing optical crosstalk, act as low-photosensitive areas and diminish overall photo-detection performance when illuminated to these areas. To overcome this issue, Microlenses are often integrated with SPAD pixels to enhance the photo detection efficiency (PDE) to collect incident photons to the photosensitive area of SPAD [3,4]. However, as SPAD pixels become more high definition, the photosensitive area is shrinking and complex shapes due to the placement of trenches and electrodes within the limited pixel space. Microlenses have limitations in optical manipulation because they rely on their curvature, which makes it difficult to focus light onto these complex photosensitive areas without complicating their design.

I proposed the monolithic integration of metalenses [5,6], which are two-dimensional flat lenses, with each corresponding SPAD pixel. This approach allows to focus incident photons on even complex photosensitive areas, simply by adjusting the positioning of the metalens structures, without the need for complex lens shapes. As a result, the fill factor and overall SiPM performance should be improved.

In this work, I first designed the optimal geometry of the metalens element and successfully fabricated a metalens array on the corresponding SPAD pixels without alignment errors. I characterized the metalens-integrated SiPM to evaluate the effectiveness of the metalens by characterizing the PDE comparing with and without the metalens. Additionally, I measured the coincident time resolution (CTR) improvement for considering the practical applications. In this talk, I introduced another nanophotonics approach tailored to different wavelengths and applications as well.

2. Method

Metasurfaces are two-dimensional arrays of sub-wavelength structures that can manipulate optical properties such as amplitude, phase, and polarization by adjusting the shape and size of the structures [7]. To achieve lens-like behavior (metalens), I designed and arranged the nanostructures accordingly. The material for the metalens must be selected based on the operating wavelength. In this research, HfO_2 was chosen due to its wide bandgap, making it highly suitable for high-transmittance optical applications without absorption at the target wavelength of 404 nm, which was specifically selected for scintillation applications such as TOF-PET and high-energy physics (HEP) experiments.

I conducted finite-difference time-domain (FDTD) simulations (ANSYS, Lumerical) to determine the optimal geometry (e.g., diameter, height) of the HfO_2 nanopillars. The period and height of the HfO_2 nanopillars were designed to be equal to or smaller than the target wavelength.

Figure 1 plots the transmittance and phase modulation as a function of the diameter of the HfO_2 nanopillars. The diameter of the HfO_2 nanopillars ranges from 80 to 230 nm, achieving 2π phase modulation with high transmittance (>80%) when the height and period are set to 480 nm and 250 nm, respectively.

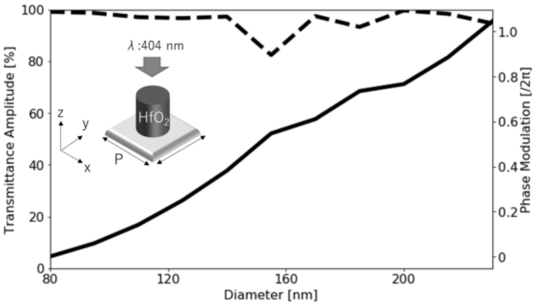

Fig. 1. The transmission (dotted line) and phase modulation (solid line) plot as a function of the diameter of the HfO_2 nanopillars at an operating wavelength of 404 nm.

3. Result

Fabrication

Figure 2(a) shows a photographic image of the metalens-integrated SiPMs used in this experiment (3 mm × 3 mm), Figure 2(b) presents a magnified view of the SiPM. As seen in Figure 2(b), 25 μm × 25 μm SPADs are arranged in a two-dimensional array, and the metalens array was successfully integrated with its corresponding SPADs without alignment errors. Figure 2(c) displays a scanning electron micrograph (SEM) image of the HfO_2 nanopillars, confirming that the nanopillars were fabricated as designed.

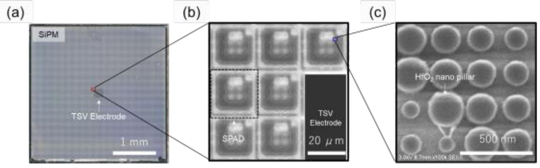

Fig. 2. (a) Photographic image of the metalens-integrated SiPM, (b) Magnified view of (a), and (c) Scanning electron micrographic (SEM) image of the HfO_2 nanopillars.

Evaluation

Figure 3 illustrates the experimental setup for characterizing the PDE of the metalens-integrated SiPM. A collimated laser (λ = 404 nm) passes through neutral density (ND) filters, reducing the light intensity to the single-photon level, and illuminates the metalens-integrated SiPM. The PDE enhancement factor was determined by comparing the PDE performance comparing with and without the metalens under applied voltage. All experiments were conducted in a dark box to eliminate any ambient light interference.

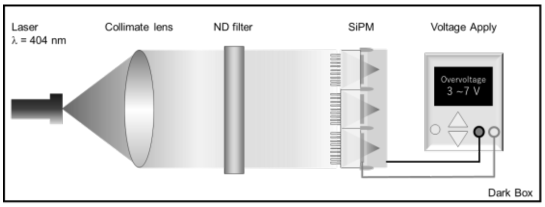

Fig. 3. Experimental set-up for characterizing the metalens-integrated SiPM.

Figure 4 plots the PDE improvement of the SPAD, comparing performance with and without the metalens, as a function of the applied voltage to the SPAD. The results demonstrate a significant improvement (~70%) at a wavelength of

404 nm across all applied voltages. Note that overvoltage refers to the voltage applied beyond the breakdown voltage, where the avalanche effect initiates at 0 V.

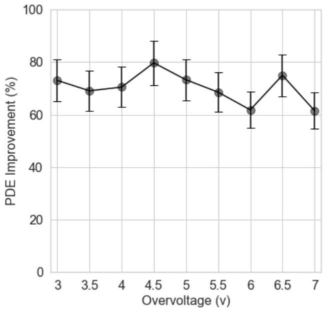

Fig. 4. Enhancement of photo detection efficiency ratio comparing with and without the metalens as a function of overvoltage. Figure shows the fabricated metalens structure.

In addition, Figure 5(a) shows the experimental setup for characterizing the coincidence time resolution (CTR) in the context of scintillation applications. A ^{22}Na radioisotope source was placed at the center between two SiPMs (Channel 1: SiPM for reference, and Channel 2: SiPM with and without the metalens). When the scintillating crystal is illuminated by the annihilation gamma rays emitted from the radioisotope source, scintillating crystals convert the gamma rays into scintillation light, which illuminates both SiPM channels. The resulting electrical signals are transmitted to an oscilloscope, where the time difference between the signals is analyzed. During the measurement, to prevent damage to the metalens, the metalens and the scintillating crystal were kept slightly separated.

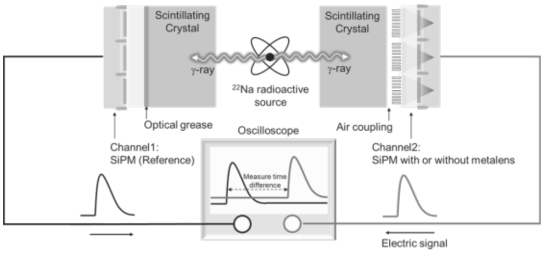

Fig. 5. Experimental set-up for characterizing the coincidence time resolution of the silicon photomultiplier with the metalens.

Figure 6(a, b) shows the histogram of the arrival time differences between the SiPM channels. I characterized the coincidence time resolution (CTR) using the full width at half maximum (FWHM) of the arrival time differences between the channels. The results demonstrated that the SiPM with the metalens improved the CTR by 54 ps compared to the SiPM without the metalens. This confirms that the metalens-integrated SiPM is effective for scintillation applications.

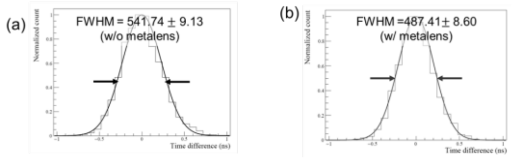

Fig. 6. CTR measurement result (a) without the metalens (b) with the metalens.

4. Discussion

In a PDE enhancement experiment for normal illumination, a significant improvement (~70%) in PDE was achieved using metalens. For the CTR measurement, the metalens-integrated SiPM demonstrated a 54 ps improvement compared to the SiPM without the metalens. It is important to note that a limitation of this experiment is that the metalens was designed for normal incidence at a wavelength of 404 nm. However, scintillation involves omnidirectional scattering and broadband wavelengths. Thus, it is essential for the metalens to be robust against varying incident angles and wavelengths. For future work, the metalens should be designed with enhanced robustness to effectively handle these challenges.

5. Conclusion

I introduced the metalens monolithically integrated with SiPM to enhance the PDE and CTR of the SiPM. I successfully fabricated the metalens with the corresponding SPAD pixel without alignment errors and demonstrated its effectiveness, achieving a 70% improvement in PDE at a wavelength of 404 nm. Additionally, the 54 ps of the CTR improvement are observed.

In this talk, I will introduce another nanophotonics approach tailored to different wavelengths such as near infrared wavelength and applications [8-10]

Acknowledgement

The author gratefully appreciates Akira Hiruma, President of Hamamatsu Photonics K. K., and Tsutomu Hara, Director of Central Research Laboratory of Hamamatsu Photonics K. K. for their supportive and heartful encouragement to perform this research.

References

[1] I. K. Sun, E. Roncali, A. Gola, G. Paternoster, C. Piemonte, S. R. Cherry, Phys. Med. Biol. 64(2019), 105007.
[2] M. Grodzicka-Kobylka, T. Szczesniak, M. Moszyński, L. Swiderski, M. Szawłowski, Nucl. Instrum. Methods Phys. Res. A 874(2017), 137.
[3] K. Otake, Y. Kitano, Y. Matsumoto, A. Yamamoto, J. Ogasahara, T. Wakano, IEEE Int. Electron Devices Meet. (IEDM) (2020), "A back-illuminated 10μm SPAD pixel array comprising full trench isolation and Cu-Cu bonding with over 14% PDE at 940nm."
[4] G. Intermite, A. McCarthy, R. E. Warburton, X. Ren, F. Villa, R. Lussana, A. J. Waddie, M. R. Taghizadeh, A. Tosi, F. Zappa, G. S. Buller, Opt. Express 23(2015), 33777.
[5] S. Uenoyama and R.Ota, ACS Photonics 8(2021), 1548–1555.
[6] S.Uenoyama and R.Ota, Advanced Optical Materials 10(2022)
[7] W. T. Chen, A. Y. Zhu, F. Capasso, Nat. Rev. Mater. 5(2020), 604.
[8] S. Uenoyama, K. Tanaka, H. Fujiwara, A. Watanabe, A. Ono, ACS Appl. Electron. Mater. 6(2024), 7046–7054.
[9] R. Ota, S. Uenoyama, Nanophotonics 12(2023), 743–752.
[10] S. Uenoyama, Y. Takiguchi, K. Takahashi, K. Hirose, H. Terada, A. Watanabe, Opt. Lett. 45(2020), 6218.

Development of Fast Scintillators Based on Hybridization of Polymer and Inorganic Nanoparticles

Masanori Koshimizu
Research Institute of Electronics, Shizuoka University
koshimizu.masanori@shizuoka.ac.jp

Abstract

Scintillators are phosphors that can be used for real-time radiation detection. Among inorganic and organic scintillators, plastic scintillators are widely used for their fast response, low production cost, and scalability. To overcome their shortcoming of low detection efficiency of X-rays and gamma rays owing to their low effective atomic numbers, nanoparticles of the heavy metal oxides have been loaded in plastic scintillators. The detection efficiency of X-rays was successfully enhanced by the loading.

1. Introduction

Scintillators are phosphors used for real-time radiation detection combined with photon detectors (photomultiplier tubes or photodiodes) in scintillation detectors. In most cases, the performance of scintillation detectors relies mostly on the scintillation properties of the scintillators. To fulfill the requirements in various applications, inorganic and organic scintillators with different compositions are commercially available. Among them, plastic scintillators have long been used in high-energy physics and monitoring of contamination of radioactive isotopes. Also, they have long been used in applications needing fast response [1].

A drawback of the plastic scintillators is low detection efficiency of X-rays and gamma rays. This is because low interaction probability of plastic scintillators with X-rays and gamma rays owing to their low effective atomic number. Plastic scintillators are composed of host polymers added with one or two kinds of organic phosphor molecules. Hence, the main elemental constituents are C, H, N, O, etc.

The effective atomic number of the plastic scintillators have long been enhanced by loading heavy metal elements as organometallic compounds. This method has two disadvantages: one is that the loading amount is limited by solubility of the organometallic compounds. The other is that the organometallic compounds act as efficient quencher, i.e., small amount of loading the compounds severely reduces the scintillation light yield.

As an alternative method, our group (and almost simultaneously a US group) proposed the loading of nanoparticles of compounds containing heavy metal elements [2]. The disadvantages of loading organometallic compounds have been overcome by using this method. In this lecture, our achievements of loading

Table 1. Detection efficiency of 67.4-keV X-rays per 1-mm thickness and scintillation light yield of SiO_2-HfO_2 nanoparticles at different amounts.

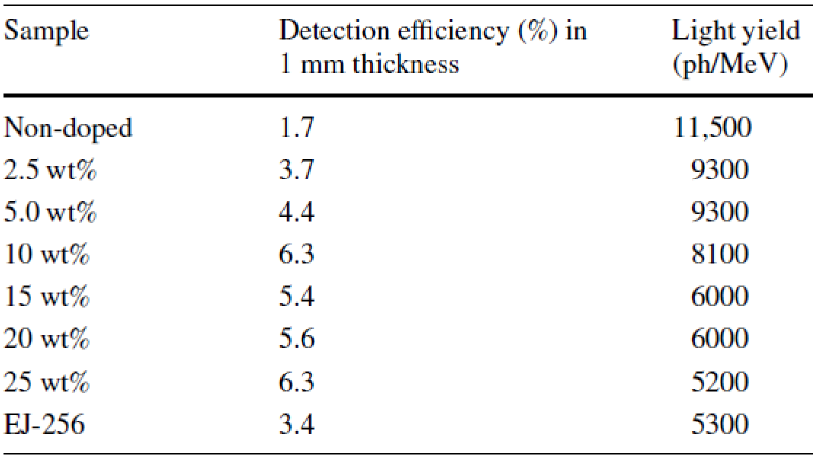

Sample	Detection efficiency (%) in 1 mm thickness	Light yield (ph/MeV)
Non-doped	1.7	11,500
2.5 wt%	3.7	9300
5.0 wt%	4.4	9300
10 wt%	6.3	8100
15 wt%	5.4	6000
20 wt%	5.6	6000
25 wt%	6.3	5200
EJ-256	3.4	5300

nanoparticles in plastic scintillators will briefly be introduced.

2. Loading Nanoparticles of Heavy Metal Oxides

At first, we have loaded SiO_2-HfO_2 nanoparticles via sol–gel method [3]. The nanoparticles were loaded in plastic scintillators composed of polystyrene host and butly-PBD as the organic phosphor. The TEM image of the plastic scintillator loaded with SiO_2-HfO_2 nanoparticles is presented in Figure 1. Nanoparticles up to 300 nm were observed. In this approach of material design, the nanoparticle size should be much less than the flight range of photoelectrons (typically > several μm). The nanoparticle size of 300 nm is appropriate from this viewpoint. The scintillators were translucent owing to the relatively large size of the nanoparticles. To obtain transparent scintillators, much smaller nanoparticles should be loaded. Subsequently, we have optimized the composition of the organic phosphors and the loaded nanoparticles. The scintillation light yields and the detection efficiency of 67.4-keV X-rays are summarized in Table 1. The scintillation light yield of 8100 photons/MeV was achieved with the nanoparticle loading amount of 10 wt%. This is 1.5 times higher than that of a commercially available plastic scintillator for X-ray and gamma-ray detection, EJ-256, which is a plastic scintillator loaded with Pb at 5 wt%. The plastic scintillator had twice the detection efficiency for 67.4-keV X-rays of that of EJ-256. This approach has also been applied to PVK-based plastic scintillators [4].

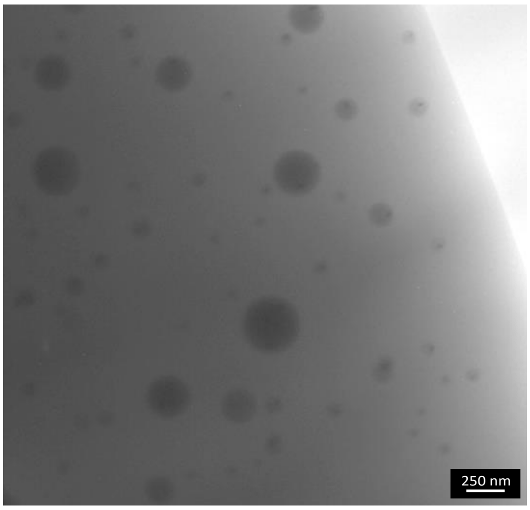

Fig. 1. TEM image of plastic scintillator loaded with HfO_2-SiO_2 nanoparticles [3].

Oxide nanoparticles have been loaded in plastic scintillators in another approach: the nanoparticles have been synthesized and subsequently loaded in plastic scintillators. At first, we used commercially available ZrO_2 nanoparticles [5]. The detection efficiency of X-rays was successfully enhanced; however, the aggregation of the nanoparticles in the plastic scintillators resulted in inhomogeneous scintillation response. Based on this experience, we developed nanoparticles using super/subcritical solvothermal synthesis method. Small nanoparticles (typically less than 10 nm) with their surface modified with organic molecules. The surface modification of the nanoparticles with organic molecules is effective to enhance the affinity of the nanoparticles with the polymer host, which results in a good dispersion of the nanoparticles within the plastic scintillators. The TEM image of the Bi_2O_3 nanoparticles synthesized in the subcritical hydrothermal synthesis method is presented in Figure 2. The average size of the nanoparticles was 4.5 nm. HfO_2 nanoparticles with similar size was also synthesized in the subcritical hydrothermal synthesis method.

We have succeeded in the synthesis of HfO_2 nanoparticles with surface modification [6]. Loading of the nanoparticle results in a significant enhancement of detection efficiency of X-rays. The plastic scintillators loaded with the HfO_2 nanoparticles combined with an avalanche photodiode were successfully used for high-energy X-ray detection of synchrotron radiation in an excellent timing resolution [7]. Also, Bi_2O_3 nanoparticles were successfully synthesized [8]. Recently, we have developed PVK-based plastic scintillators

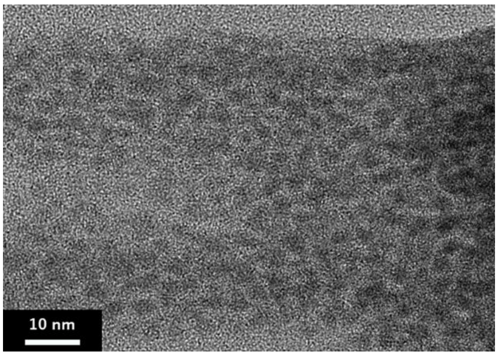

Fig. 2. TEM image of Bi_2O_3 nanoparticles synthesized in subcritical hydrothermal method [8].

loaded with Bi_2O_3 nanoparticles exhibiting high performance: using a combination of PVK host and DPA as the organic phosphor had the scintillation light yield and detection efficiency of the 67.4-keV X-rays twice those of EJ-256.

3. Loading Halide Quantum Dots

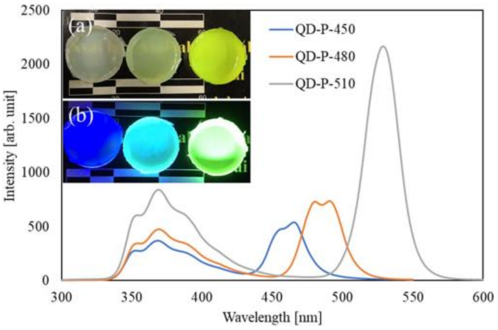

Figure 3. Photoluminescence spectra of plastic scintillators loaded with QD-P-450, QD-P-480, and QD-P-510, with excitation at 250 nm. The insets are photographs of the plastic scintillators loaded with QD-P-450, QD-P-480, and QD-P-510 (from left to right), (a) under visible light and (b) 254 nm ultraviolet irradiation.

In Chapter 2, development of plastic scintillators loaded with non-emissive nanoparticles was introduced. This is mainly because we developed the nanoparticle-loaded plastic scintillators having fast response and high detection efficiency of X-rays: if the loaded nanoparticles exhibit efficient scintillation with a long decay, the fast response of the plastic scintillators cannot be fully exploited. If we load emissive nanoparticles to plastic scintillators to obtain fast scintillators, nanoparticles exhibiting fast emission should be loaded. From this viewpoint, perovskite quantum dots (QDs) are appropriate to be loaded in plastic scintillators. We have developed emissive perovskite QD-loaded plastic scintillators [9]. Their photoluminescence excitation and emission spectra are presented with their photographs. Both emission from the loaded QDs and the organic phosphor (butyl-PBD) can be seen. On the contrary to our expectation, the loading of the emissive perovskite QDs significantly reduced the scintillation light yield. The cause of this reduction is self-absorption of the scintillation inside the scintillators: because the Stokes shift of the perovskite QDs is small, the emission of a perovskite QD is effectively absorbed by another perovskite QD nearby. The repetition of this process results in a severe reduction in the scintillation light yield.

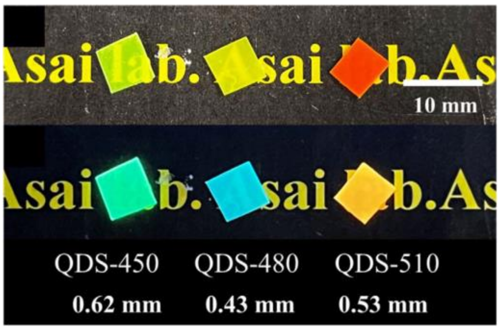

Figure 4. Photographs of sample scintillators under (a) room lighting and (b) UV light at 365 nm.

To avoid the self-absorption, wavelength shifting molecules were added to the plastic scintillators loaded with the perovskite QDs [10]. Their photographs are presented in Figure 4. This was partially successfully; however, the enhancement in the scintillation light yield was difficult. The scintillation light yields of the samples without and with the

Table 2. Scintillation light yields of plastic scintillators loaded with perovskite QDs without and with the wavelength shifting molecules.

Sample	Scintillation light yield (photons MeV^{-1})
Polystyrene + butyl-PBD + QD-P450	2500
QDS-450 (Polystyrene + butyl-PBD + QD-P450 + Coumarin 6)	4200
Polystyrene + butyl-PBD + QD-P480	2900
QDS-480 (Polystyrene + butyl-PBD + QD-P480 + BPEA)	—
Polystyrene + butyl-PBD + QD-P510	2900
QDS-510 (Polystyrene + butyl-PBD + QD-P510 + Nile red)	3200

wavelength shifting molecules are summarized in Table 2.

4. Conclusions and Future Prospects

As a new class of scintillators, our achievements of nanoparticle-loaded plastic scintillators are introduced. Loading nanoparticles of heavy metal oxide were successful. In particular, super/subcritical hydrothermal synthesis is a powerful method to fabricate nanoparticles to be loaded in plastic scintillators. On the contrary, loading emissive nanoparticles is difficult to achieve high scintillation light yield. In near future, the self-absorption of the QDs owing to the small Stokes shift should be avoided by using some energy transfer process.

References

[1] Masanori Koshimizu, Jpn. J. Appl. Phys. **62** (2023) 010503.

[2] Masanori Koshimizu, Funct. Mater. Lett. **13** (2020) 2030003.

[3] Y. Sun et al, Appl. Phys. Lett. **104** (2014) 174104.

[4] Atsushi Sato, Masanori Koshimizu, Yutaka Fujimoto, Shunji Kishimoto, Keisuke Asai, J. Mater. Sci. Electron. **32** (2021) 28807.

[5] Yuki Araya, Masanori Koshimizu, Rie Haruki, Fumihiko Nishikido, Shunji Kishimoto, Keisuke Asai, Sensors and Materials, **27** (2015) 255.

[6] Fumiyuki Hiyama, Takio Noguchi, Masanori Koshimizu, Shunji Kishimoto, Rie Haruki, Fumihiko Nishikido, Takayuki Yanagida, Yutaka Fujimoto, Tsutomu Aida, Seiichi Takami, Tadafumi Adschiri, Keisuke Asai, Jpn. J. Appl. Phys., **57** (2018) 012601.

[7] K. Inoue, M. Koshimizu, F. Hiyama, K. Asai, F. Nishikido, R. Haruki, S. Kishimoto, IEEE Trans. Nucl. Sci. **65** (2018) 1012.

[8] Fumiyuki Hiyama, Takio Noguchi, Masanori Koshimizu, Shunji Kishimoto, Rie Haruki, Fumihiko Nishikido, Yutaka Fujimoto, Tsutomu Aida, Seiichi Takami, Tadafumi Adschiri, and Keisuke Asai, Jpn. J. Appl. Phys. **57** (2018) 052203.

[9] Arisa Magi, Masanori Koshimizu, Atsushi Sato, Yutaka Fujimoto, Shunji Kishimoto, Takayuki Yanagida, Keisuke Asai, Jpn. J. Appl. Phys. **62** (2022) SB1036.

[10] Atsushi Sato, Yutaka Fujimoto, Keisuke Asai, Masanori Koshimizu, Jpn. J. Appl. Phys. **63** (2024) 01SP06.

Tuning the functional properties of nanostructures materials for highly efficient optoelectronic devices

Mani Navaneethan
Nanotechnology Research Centre,
Faculty of Engineering and Technology,
SRM Institute of Science and Technology, India
m.navaneethan@gmail.com

Abstract

Tailoring the optoelectronic characteristics of different nanomaterials (TiO_2, PbS, CdS, ZnSe, $CuInS_2$, MnS, ZnS, and ZnSe) for vibrant electronic applications is a field in which I have vast research experience. Optical bandgap, surface morphology, intrinsic band structure, and other factors are some of the factors that affect a material's optoelectronic properties. Through a variety of techniques, I have meticulously adjusted each of these parameters independently, producing exceptional outcomes. For example, because of its high carrier mobility and robust light-matter interaction, two-dimensional molybdenum disulfide (MoS_2) presents a great potential for next-generation photodetectors. However, problems like Fermi level pinning and surface defects may limit its photo response properties, particularly in the near-infrared (NIR) region. The aim of this work is to investigate how the optoelectronic properties of few-layer MoS_2 can be improved for NIR photodetection by varying the Fermi energy through metal passivation (iron and zinc). Significant improvements in photocurrent, spectral response, and external quantum efficiency (EQE) were observed by using chemical vapor deposition (CVD) to fabricate few-layer MoS_2 photodetectors, followed by surface passivation with zinc (Zn) and iron (Fe). In the near infrared (NIR) range, Zn-passivated MoS2 demonstrated a photocurrent of 5.79×10^{-6} A and a remarkable spectral responsivity of 1450 mA/W, significantly surpassing that of unmodified MoS_2 (188 mA/W). Its potential for sensitive detection in NIR applications like optical communications and surveillance systems is highlighted by the detectivity's increase to 1.28×10^{12} jones. This improvement was largely due to the suppression of Fermi level pinning via surface passivation, which decreased surface defects and raised the Zn-MoS2 Schottky barrier height (SBH) to 0.39 eV. This resulted in quicker photo response times and more effective charge separation. Further enhancing the optoelectronic performance was the tensile strain brought about by metal passivation, as evidenced by the increased EQE (30 % for Zn-MoS_2) and large Seebeck coefficient (-45 mV/K). According to this work, MoS_2-based photodetectors can perform much better when their metal passivation strategies are well-designed. This makes them a great choice for NIR optoelectronic applications.

1. Introduction

Thanks to their high planar mobility, two-dimensional (2D) materials have become attractive candidates for photodetectors. For instance, graphene provides 20,000 cm^2/Vs; however, its application is limited by its high dark current and absence of bandgap. The superior photoresponse of molybdenum disulfide (MoS_2), which has a structure resembling graphene and is distinguished by high exciton binding energies, strong light-matter interaction, and mechanical flexibility, has drawn attention. However, MoS_2-based photodetectors have limitations due to their low bandwidth, slow response time, and high dark current. These can be lessened by using techniques like molecular physisorption, surface modification, and gate biasing.

Advancements in recent times have concentrated on changing the number of layers and using heterostructures to maximize the performance of MoS_2. MoS_2 photodetectors on substrates such as Al_2O_3 and HfO_2 have demonstrated responsivity between 10^3 and 10^4 A/W and detectivity between 10^9 and 10^{11} Jones. While photoresponse has been improved by a variety of heterostructures, such as van der Waals (graphene, $SnSe_2$) and perovskite, stability and cost issues still exist.

Photoresponse can be enhanced and dark current suppressed by forming p-n junctions, such as MoS_2 with MnO. Furthermore, Schottky barrier junctions and MoS_2-Au hybrid structures (e.g. G. Pt/MoS_2) have demonstrated the ability to improve optoelectronic characteristics. For example, I used a hydrothermal method to successfully synthesize Al-doped TiO_2 embedded graphene oxide and found that by mitigating defects, metal doping into the TiO_2 matrix greatly enhanced its optical properties. The Al doped TiO_2-GO nanocomposite's improved charge transport was shown in a study that was published in ***Applied Surface Science, 449 (2018) 332-339***. In a similar manner, I demonstrated CdS nanoflowers using a capped PVP that was created by carefully regulating the temperature and reaction time. The material's band structure changed as a result of the phase transition from cubic to hexagonal. UV-vis absorption spectroscopy revealed improved optical characteristics of CdS nanoflowers as a result (***Materials Research Bulletin, 94 (2017) 190-198***). I have also investigated the synthesis of $CuInS_2$/MnS/ZnS core-multishell nanocrystals using a hot injection method, which resulted in enhanced stability at 543 and 752 nm, in addition to the typical nanostructures. Optical and structural characterization techniques demonstrated the important utility of nanocrystals as an effective bioimaging probe (***Ind. Eng. Chem. 15703–157721, Res, 57 (2018)***). Accordingly, PbS nanocubes made using a wet chemical method were the subject of the study. Through meticulous manipulation of the temperature and reaction duration, I was able to produce monodispersed nanocubes with sizes between 10 and 15 nm. In order to effectively utilize quantum confinement effects, these nanocubes were purposefully made smaller than the excitonic Bohr radius of bulk PbS. Promising findings from this study can be actively incorporated into optoelectronic industry applications in the future (***Materials Letters, 71 (2012*** 44–47). I carried out a number of studies on modifying the shape of nanomaterials using various techniques to improve their optical characteristics. For example, I experimented with the one-step chemical synthesis of CdS nanospheres devoid of surfactants and adjusted their shape by varying the concentration of thioacetamide (C_2H_5NS). By altering the concentration of C_2H_5NS, CdS sphere shapes changed, and the band gap shrank from 2.44 to 2.22 eV, improving optical characteristics (***Superlattices and microstructure, 104 (2017) 247-257***). Additionally, I looked into the optical characteristics of ZnS nanostructures that were created by a wet chemical process and then annealed at various temperatures. I was able to control the morphology and change the nanostructures from nanoparticles to nanorods by varying the annealing temperature. Notably, the quantum con was blamed for the observed shift in absorption edge wavelengths.

This work explores surface passivation of MoS_2 with metals like Zn and Fe to increase Schottky barrier height, reduce Fermi level pinning, and enhance optoelectronic properties. The results demonstrate improved detectivity and photoresponse for NIR applications, offering a promising pathway for next-generation photodetectors.

2. Results and Discussion

The two characteristic Raman peaks of MoS_2 observed at 382.9 cm^{-1} and 408.8 cm^{-1} correspond to the in-plane vibration mode (E_1^2g) and out-of-plane vibration mode (A_1g), respectively. These peaks are indicative of the formation of bulk MoS_2 layers, as their position closely matches previously reported values for multilayer MoS_2.The E^1_2g mode represents the vibration of Mo and S atoms in opposite directions within the same layer, while the A_1g mode reflects the vibrations of S atoms perpendicular to the layers. Upon Zn passivation, the peaks shifted to 379.4 cm^{-1} (E^1_2g) and 405.3 cm^{-1} (A_1g). This red shift indicates a reduction in the phonon energy, commonly attributed to the introduction of tensile strain. Tensile strain typically elongates the bonds in the lattice structure, reducing the vibrational frequency and leading to this downward shift in the

Raman peaks. Zn atoms may have intercalated or adsorbed onto the MoS_2 surface, stretching the lattice structure and inducing strain. In contrast, for Fe-passivated MoS_2, only the A_1g mode shifted slightly to 407.8 cm^{-1}, with no significant shift in the E^1_2g mode. This selective shift suggests that Fe passivation primarily affects the out-of-plane vibrations rather than the in-plane vibrations. One possible explanation is that Fe atoms interact more strongly with the sulfur atoms at the surface, altering the out-of-plane vibrations without significantly affecting the in-plane dynamics. The increased A_1g/E^1_2g intensity ratio with metal passivation, particularly with Fe and Zn, implies an enhanced phonon population in the out-of-plane vibrational mode. This could result from changes in electronic structure or surface interactions induced by metal passivation. The higher intensity of the A_1g peak suggests stronger interactions in the out-of-plane direction, possibly due to metal adsorption enhancing the layer-layer coupling or modifying the surface electron-phonon interactions. Field emission scanning electron microscopy (FESEM) images confirmed that the MoS_2 maintained a sheet-like morphology post-metal passivation, suggesting that the metal deposition did not destroy the 2D layered structure.

Elemental mapping confirmed the presence of Mo, S, Si, and Ag within the device, validating the presence of MoS_2 and the additional elements possibly introduced during device fabrication or metal passivation. The uniform distribution of these elements indicates successful incorporation of metal species (Zn or Fe) into the MoS_2 structure or on its surface, consistent with the Raman shifts observed.

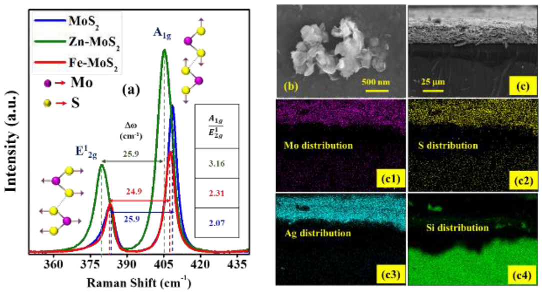

Fig. 1. Micro-Raman spectra of MoS_2, Zn-MoS_2 and Fe- MoS_2 (a), FESEM (b), cross section FESEM (c), Elemental distribution of cross section FESEM mapping Mo (c1), S (c2), Ag (c3) and Si (c4) of MoS_2.

The current-voltage (I-V) characteristics of MoS_2, Zn-MoS_2, and Fe-MoS_2 were measured under both dark and illumination conditions. Zn-MoS_2 showed the highest dark current (3.98 × 10^{-6} A) and illuminated current (9.77 × 10^{-6} A), indicating enhanced carrier injection due to surface passivation. Fe-MoS_2 demonstrated improved performance compared to unmodified MoS_2 but lower than Zn-MoS_2. The improved photodetection was attributed to the reduction in fermi level pinning (FLP) by Zn and Fe passivation, which reduced surface states and enabled better carrier flow.

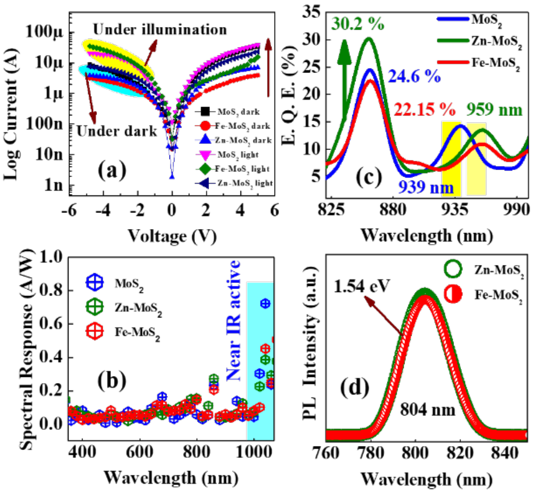

Fig. 2. Semi-log (I-V) characteristics under dark and illumination (a), wavelength vs spectral response (b), wavelength vs external quantum efficiency (E. Q. E) (c) of MoS_2, Zn-MoS_2 and Fe- MoS_2 (d) PL emission spectra Zn- MoS_2 and Fe- MoS_2.

The spectral response (R_λ) was measured across 300–1100 nm, with maximum response above 860 nm, indicating the devices' capability in the near-infrared (NIR) range. R_λ values were 188 mA/W for MoS_2, which drastically increased to 1450 mA/W for Zn-MoS_2 and 1220 mA/W for Fe-MoS_2. The Zn-passivated MoS_2 device showed an 87%

enhancement in R_λ compared to previously reported devices. The enhancement was attributed to increased photo-charge carrier generation. External quantum efficiency (η_{EQE}) of the devices was also enhanced, with Zn-MoS_2 showing the highest efficiency of 30.2%.

Photoluminescence (PL) spectra for Zn-MoS_2 and Fe-MoS_2 showed a strong emission at 1.54 eV. No significant shift in emission spectra was observed, but the reduction in PL intensity was associated with surface passivation and tunneling of charge carriers. The reduced band bending energy due to tensile strain in Zn-MoS_2 facilitated the separation of photo-generated electron-hole pairs, leading to enhanced photoconduction properties. The quantum confinement effect was observed in the perpendicular direction of MoS_2 layers.

Cyclic I-V measurements in the dark and under illumination showed enhanced photoconduction in the passivated devices. The presence of surface traps and their role in charge trapping and detrapping were confirmed by PL and I-V hysteresis. Zn passivation created a tensile strain that prolonged photoresponse time, improving photocurrent, spectral response, and external quantum efficiency. The I-V characteristics confirmed better photoconduction in Zn-MoS_2 devices, with photocurrent increasing from 1.8×10^{-6} A to 2.7×10^{-6} A as the wavelength increased from 840 nm to 1080 nm. Temporal photoresponse measurements at different voltages confirmed the superior performance of Zn-MoS_2, showing faster rise (τ_r) and decay times (τ_d) than MoS_2 and Fe-MoS_2. For Zn-MoS_2, τ_r and τ_d were calculated as 1.3 and 1.2 s, respectively. The detectivity (D_t) is calculated using,

$$D_t = \frac{R_\lambda A^{1/2}}{(2qI_{dark})^{1/2}},$$

where q is electron charge (i.e., 1.6×10^{-19} C). The detectivity (D_t) was significantly higher in Zn-MoS_2 and Fe-MoS_2 (1.28×10^{12} jones) compared to MoS_2 (2.64×10^{11} jones), indicating enhanced photodetection ability due to better passivation and surface trap states.

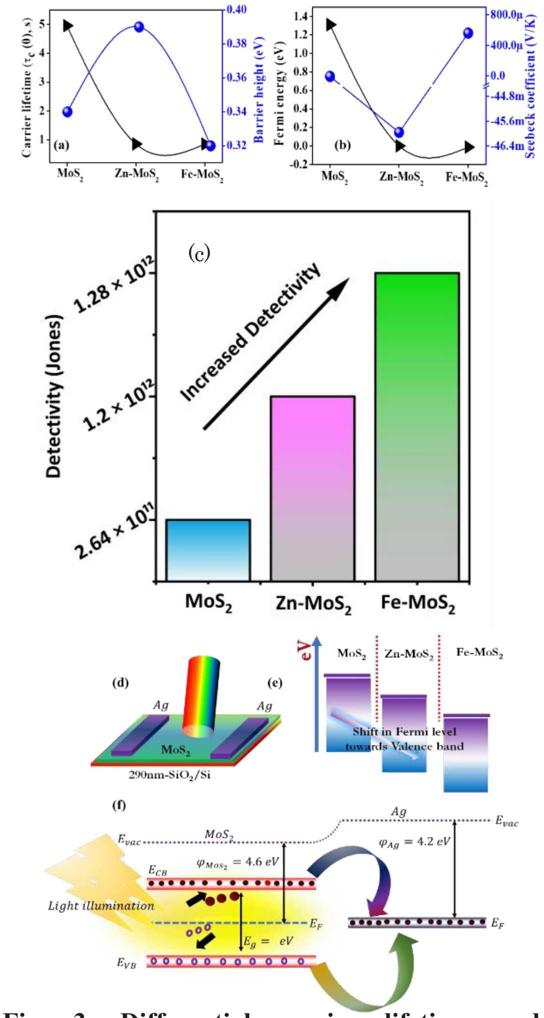

Fig. 3. Differential carrier lifetime and Schottky barrier height (a), Fermi energy and Seebeck coefficient (b) of MoS_2, Zn- MoS_2 and Fe- MoS_2, Literature survey (c), Schematic illustration of device scheme (d), Fermi energy shift near valence band by (Zn & Fe) passivation in MoS_2 (e), Charge transfer at the interface of Ag and MoS_2 (f).

In this present work Zn and Fe passivation on MoS_2 notably tailored the discrete trapping traps and the carrier lifetime which enhance its photo switching behavior with sharp rise and decay. However, the decay curve in the temporal response shows the differences in slopes with different cycles of measurements confirms the presence of traps mediated energy gap. The existence of traps leads to an increase the lifetime of generated current carriers which influences in the decay time of the photocurrent. According to the Fuhs-Stuke concepts [37], the differential lifetime of the generated current carriers is calculated from the relation,

$$\tau_c = \frac{1}{\left(\frac{1}{I_{ph}(0)}\frac{dI_{ph}(t)}{dt}\right)}$$

where τ_c is the differential current carrier lifetime,

$$\frac{dI_{ph}(t)}{dt}$$

is the decay rate and $I_{ph}(0)$ is the steady state photocurrent. The τ_c at t=0 are 4.957, 0.854 and 0.851 for MoS_2, Zn-MoS_2 and Fe-MoS_2, respectively, thus the low τ_c of Zn-MoS_2 indicates better photoconductivity.

The temperature-dependent I-V characteristics followed the Richardson-Dushman thermionic emission theory. The Schottky barrier height (φ_{b0}) values were calculated as 0.34 eV, 0.39 eV, and 0.32 eV for MoS_2, Zn-MoS_2, and Fe-MoS_2, respectively, suggesting reduced FLP with metal passivation. Fermi energy (EF) was also calculated, showing a significant downshift towards the valence band (VB) for Zn-MoS_2, confirming effective suppression of FLP.

Zn-MoS_2 exhibited superior photodetector performance, with the highest detectivity and external quantum efficiency among the three devices. The observed enhancement in NIR response (>860 nm) was due to efficient passivation, reduced surface trap states, and increased charge carrier generation. Zn-MoS_2 outperformed Fe-MoS_2 due to greater tensile strain and better suppression of surface defects, which improved carrier mobility and photodetector responsiveness.

3. Conclusion

In conclusion, Zn-passivated MoS_2 photodetectors showed significant enhancement in photocurrent, spectral response, and detectivity compared to Fe-passivated and unmodified MoS_2. The surface passivation by Zn created tensile strain, which reduced FLP and improved the photo-switching behavior of the device, making it highly effective in the NIR range. The findings demonstrate the potential for further optimization of MoS_2-based photodetectors for applications in NIR sensing and imaging.

References

[1] Prabakaran, S., K. D. Nisha, S. Harish, J. Archana, **M. Navaneethan**, S. Ponnusamy, C. Muthamizhchelvan, and Y. Hayakawa. "Effect of Al doping on the electrical and optical properties of TiO2 embedded Graphene Oxide nanosheets for opto-electronic applications." Applied Surface Science 449 (2018): 332-339.

[2] Renuga, V., C. Neela Mohan, MS Mohamed Jaabir, P. Arul Prakash, and **M. Navaneethan**. "Synthesis and Surface Passivation of CuInS2/MnS/ZnS Core–Multishell Nanocrystals, Their Optical, Structural, and Morphological Characterization, and Their Bioimaging Applications." Industrial & Engineering Chemistry Research 57, no. 46 (2018): 15703-15721.

[3] R. Abinaya, E.Vinoth, S.Harish, S.Ponnusamy, J, Archana; M Shimomura, **M. Navaneethan**, M. Modulating Fermi energy in few layer MoS2 via metal passivation with enhanced detectivity for Near IR Photodetector, J. Mater. Chem. C, 12 (2024) 5247-5256.

[4] Vinoth Elangovan, Vijay Vaiyapuri, R Aysha Parveen, Archana Jayaram, Harish Santhanakrishnan, **Navaneethan Mani**, A silver nanoparticle (AgNP)-loaded Bi2Se3 topological insulator p-n heterojunction photodiode for a near-infrared (NIR) photodetector, Nano Futures, (2023) 7(2), 025004.

[5] E.Vinoth, J.Archana , S.Harish, and **M.Navaneethan**, Hydrothermally derived layered of 2D SnS nanosheets for Near Infra-Red (NIR) photodetectors. IEEE Photonics Technology Letters (99) (2021) 1-1.


SHIZUOKA UNIVERSITY
RESEARCH INSTITUTE OF ELECTRONICS
1924
1965


大學